REMOTE, NON-INVASIVE, OPTICAL METHOD

OF TEMPERATURE DETECTION

by

Travis Hugh Hutchins, B.S.

A thesis submitted to the Graduate Council of
Texas State University in partial fulfillment
of the requirements for the degree of
Master of Science
with a Major in Physics
May 2015

Committee Members:

Mark Holtz, Chair

Thomas Myers

David Donnelly

FAIR USE AND AUTHOR'S PERMISSION STATEMENT

Fair Use

Duplication Permission

DEDICATION

I dedicate this thesis to my parents, Shana and Lauren.

ACKNOWLEDGEMENTS

I would like to thank my thesis adviser, Professor Mark Holtz, for his patience, insight, and support. I'd also like to thank Bobby Hancock and Dr. Mohammed Nazari for their help and technical support in lab. Included in my acknowledgements are Professor Thomas Myers for his permission to use the MBE system, as well as Dr. Madhavie Edirisooriya for her assistance with MBE operations. Finally, I'd like to think Professor Michelle Londa for her inspiration, guidance, and encouragement.

TABLE OF CONTENTS

Page

LIST OF TABLES

Table **Page**

LIST OF FIGURES

Figure **Page**

ABSTRACT

The focus of this thesis is the development of a remote, optically based, non-invasive, large working distance Raman method of temperature detection that relies upon observing the temperature-dependent phonon redshift. The method was applied to detect in-situ temperatures of a molecular beam epitaxy (MBE) system's sample manipulator during a standard ramp process. The development process entailed calibrating measurements of the E_2 Raman peak of test subject 6H-SiC with thermocouple temperatures in a standard laboratory setting and at two known melting points, In and InSb, in the MBE chamber. A key part of this method's development was designing an apparatus capable of acquiring Raman spectra at the sample-optical port separation distance found in the MBE chamber. Available capabilities permitted the qualification of this approach from room temperature to 527 °C. Comparing the redshift predicted by the combined effects of thermal expansion and anharmonic phonon decay with the calibration data yielded fit parameters that are in good agreement with what has been previously reported. Results show that the thermocouple significantly overestimates the substrate temperature by approximately 100 °C and that there is a > 10 min delay in achieving steady state at the sample relative to the controller.

1. INTRODUCTION

The topic of this thesis is the development of an optically based, non-invasive method of remote temperature detection. An ability to obtain accurate temperature measurements is required in the field of material science and by the semiconductor industry. In a vacuum chamber designed for Molecular Beam Epitaxy (MBE), a process common to material science, substrate temperatures were inferred using the Raman spectra of 6H-SiC. The efforts described in the following work conclude that it is possible to obtain in-situ, real-time temperature measurements of an MBE sample holder by observing the temperature-dependent redshift and broadening of the E_2 Raman peak of 6H-SiC.

2. MOLECULAR BEAM EPITAXY

Molecular Beam Epitaxy (MBE) is an ultra high vacuum process used to grow films of semiconducting materials. Film growth is accomplished by directing beams of atoms or molecules on to a substrate where they react to form epitaxial layers. These systems commonly include a growth chamber (Fig. 1a), an auxiliary chamber containing analytical tools, a buffer chamber for pre-growth processing, and load locks for substrate (sample) entry and exit.[1] Growth chambers typically feature beam sources, a residual gas analyzer to monitor beam and background gas compositions, a RHEED (reflection high energy electron diffraction) system, and a heated sample manipulator (Fig. 1b). Samples are introduced into an MBE system by mounting them on to holders that mechanically lock with each transport mechanism.

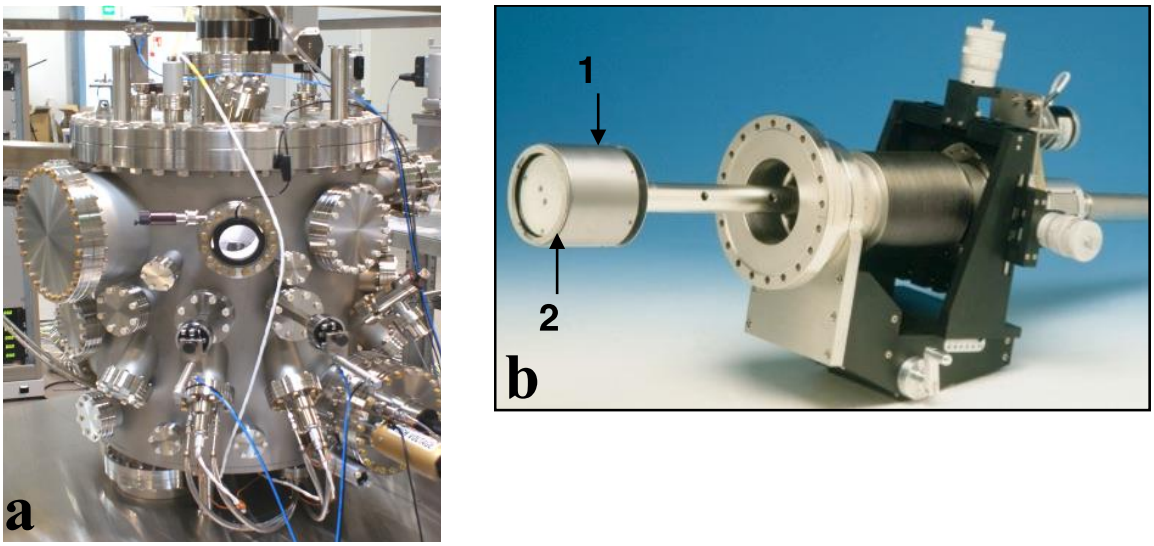

Figure 1: MBE System. (a) DCA-M600 MBE growth chamber, (b) manipulator arm with heater housing 1 and sample holder receiver 2 (dca.co.uk).

A common practice is to use a holder machined from a molybdenum block and mount samples using indium solder or, if composition prohibits, by mechanical means. Indium has a melting point of 156.6°C,[2] which renders the solder in a liquid state for most temperatures encountered in MBE growth. Indium solder in liquid form provides sufficient sample-holder adhesion and increases thermal contact.[1]

The production of high quality, uniform epitaxial layers requires a manipulator that can translate, rotate, and uniformly heat growth substrates (Fig. 1b). Sample heat is typically provided by a resistive element.[3] The element is recessed within the manipulator housing, and as power is supplied it radiates heat towards the substrate. A thermocouple that is either in contact or located near the sample holder, on the opposite side of the sample, relays temperature data to a proportional-integral-derivative (PID) loop which controls heating power.

Due to its recessed location, the thermocouple of an MBE manipulator can only maintain sample temperature and not provide an absolute reading. This inherent inaccuracy can be bypassed by calibrating thermocouple readings with alloy eutectic points and the temperature at which the oxide desorption of GaAs occurs, 582°C.[3,4] Optical pyrometry offers an accurate method of sample temperature determination, however it is limited to temperatures above 400 °C and is dependent on the interrogated material's emissivity.

More sophisticated optical approaches for measuring temperature inside an MBE system have been developed. Among these are techniques based on the temperature dependence of the semiconductor band edge for the material being deposited[5] and reflectance anisotropy spectroscopy.[6] While each of these methods has its merits, one consideration is the need to know what material is deposited and its temperature-dependent optical properties in the temperature range of interest, limitations in temperature range addressable, and applicability to an arbitrary material.

Raman spectroscopy is a viable approach for determining absolute temperature of a substrate or epitaxial layer for a broad range of materials. The typically narrow Raman bands systematically shift and broaden with increasing temperature and the dependence has been established for many materials. A perceived difficulty in using Raman scattering to examine materials *in situ* is the typically weak signals and the consequent need to use collection optics with high numerical aperture. Despite these factors, progress has been made in measuring Raman spectra with large working distance optics.[7] However, the majority of Raman applications are devoted to the study of epitaxial material and the monitoring of semiconductor process parameters has not yet been fully exploited.[8] In this work it is demonstrated that conventional optics and commonly available Raman instrumentation permit measurement of temperature in a working MBE system and across a wide temperature range.

3. CRYSTALS

The remote, non-invasive, Raman spectroscopy-based method of determining MBE temperatures was carried out using a 6H-SiC substrate, which is a crystalline material that is further described in section 6.1. Chapter 3 gives a basic overview of the properties of crystals, including their basic structure and varieties of symmetry.

3.1 Crystal Structure

A crystal can be described in terms of a 3D periodic array of points in space with a collection of atoms identically attached to each point. The 3D periodic array of points is known as a lattice and the collection of atoms is known as a basis.[9]

Associated with each lattice are three fundamental translation vectors $\mathbf{a_1}$, $\mathbf{a_2}$, $\mathbf{a_3}$ such that the configuration of atoms looks identical in every respect when observed from the point **r** as when observed from the point

$$\mathbf{r'} = \mathbf{r} + u_1\mathbf{a_1} + u_2\mathbf{a_2} + u_3\mathbf{a_3} \quad (1)$$

where u_1, u_2, u_3 are arbitrary integers. The set of points given by Eq. (1) defines a lattice.[9]

The lattice and translation vectors $\mathbf{a_1}$, $\mathbf{a_2}$, $\mathbf{a_3}$ are called primitive if any two points **r**, **r'** from which the configuration of atoms appears identical always satisfies Eq. (1) for an appropriate choice of integers u_1, u_2, u_3. The primitive translation vectors are frequently used to define the axes of a crystal and form three adjacent edges of a parallelepiped. The parallelepiped is known as a primitive cell if there are lattice points

located only at its corners, and the lengths of the crystal axes and the angles between them are characteristic to each lattice.[9]

A primitive cell is associated with a single lattice point, and contains the minimum number of atoms needed to from the crystal structure when translated along the crystal axes. The number of atoms contained within a primitive cell is always identical for a given crystal structure.[9]

Crystals of certain compositions, such as ZnS and SiC, exhibit different crystal structures for the same set of atomic constituents, known as polytypism. Polytypism occurs when crystal structures of a given composition differ by the sequence in which atoms are stacked within the primitive cell.[9]

As is evident from Eq. (1), infinite repetitions of a primitive cell imply that all crystals possess translational symmetry. The position in one primitive cell is identical to a position in another primitive cell under a lattice translation operation **T** defined as

$$\mathbf{T} = u_1\mathbf{a_1} + u_2\mathbf{a_2} + u_3\mathbf{a_3} \tag{2}$$

where u_1, u_2, u_3 are constants representing the integer number of lattice vectors a given position is translated.[9] In the physics of lattice dynamics, a position dependent quantity may be uniquely specified up to **T**.

Along with a crystal lattice, each crystal is associated with a reciprocal lattice. The reciprocal lattice is defined by the primitive vectors $\mathbf{b_1}$, $\mathbf{b_2}$, $\mathbf{b_3}$ which satisfy

$$\mathbf{b_i} \circ \mathbf{a_j} = 2\pi\delta_{ij} \tag{3}$$

and are defined as

$$\mathbf{b_i} = 2\pi \frac{\mathbf{a_j} \circ \mathbf{a_k}}{\mathbf{a_i} \circ \mathbf{a_j} \times \mathbf{a_k}} \tag{4}$$

where a_i are the previously mentioned primitive translation vectors, and have the dimensions of (1/[length]).[9] Defining a reciprocal lattice becomes necessary when dealing with quantities that depend on wavevectors or when analyzing the kinematics of interactions that occur within a crystal.

The reciprocal lattice analog of the primitive cell is what is commonly known as the first Brillouin zone. It is defined by constructing a Wigner-Seitz cell in reciprocal space using the primitive vectors $\mathbf{b_1}$, $\mathbf{b_2}$, $\mathbf{b_3}$. In reciprocal space, a Wigner-Seitz cell is the region formed from the intersection of planes that normally intercept and bisect $\mathbf{b_i}$. The first Brillouin zone (BZ) is defined to be the Wigner-Seitz cell constructed with the nearest neighboring points about the primitive cell's origin in reciprocal space.[9] All of the information concerning the momentum and energy of interactions occurring within the periodic potential of a crystal are specified within the boundaries of the first Brillouin zone.

Furthermore, the reciprocal lattice analog of the translation vector **T** is the reciprocal lattice vector **G** defined as

$$\mathbf{G} = v_1\mathbf{b_1} + v_2\mathbf{b_2} + v_3\mathbf{b_3} \tag{5}$$

where v_1, v_2, v_3 are integers. Wavevectors in the reciprocal lattice, and the quantities which depend on them, may be uniquely specified up to **G** such that

$$\mathbf{k} + \mathbf{G} = \mathbf{k} \tag{6}$$

for any wavevector **k** and all **G** defined by Eq. 5.[9]

Table 1: Symmetry Element Notations [9]

Symmetry Element	Schönflies Notation	International (Hermann-Mauguin)
Identity	E	1
Rotation axes	C_n	$n = 1, 2, 3, 4, 6$
Mirror planes	σ	m
$\perp$ to n-fold axis	σ_h	m, m_z
$\parallel$ to n-fold axis	σ_v	$m_{v'}$
bisecting $\angle$	σ_d	m_d, m'
Inversion	I	$\bar{1}$
Rotoinversion axes	S_n	$n = \bar{1}, \bar{2}, \bar{3}, \bar{4}, \bar{6}$
Translation	t_n	t_n
Screw axes	C_n^k	n_k
Glide planes	σ^g	a, b, c, n, d

3.2 Crystal Symmetry

The types of symmetry associated with a crystal lattice are exemplified by symmetry operations such as rotation, mirror reflection, inversion, and the previosly mentioned translation. Symmetry operations are applied about a lattice point and the collection of symmetry operations that leave a lattice unchanged are known as a lattice point group, which is a concept pertaining to the mathematical field of group theory. The

symmetry operations are known as elements and their definitions are listed in two common notation schemes in Table 1.

The symmetry operations applicable to lattices existing in 3D space require 14 different lattice types which are grouped into 7 systems. Each crystal system defines a set of primitive cell shapes and the relations between crystal axes and primitive cell angles. The specifics of each system are detailed in Table 2, with the crystal axes notation becoming $a_1 \rightarrow a,\ a_2 \rightarrow b,\ a_3 \rightarrow c$.

Table 2: Three Dimensional Crystal Systems [9]

Crystal System	**Axial Relationships**	**Interaxial Angles**
Cubic	$a = b = c$	$\alpha = \beta = \gamma = 90°$
Hexagonal	$a = b \neq c$	$\alpha = \beta = 90°, \gamma = 120°$
Tetragonal	$a = b \neq c$	$\alpha = \beta = \gamma = 90°$
Rhombohedral (Trigonal)	$a = b = c$	$\alpha = \beta = \gamma \neq 90°$
Orthorhombic	$a \neq b \neq c$	$\alpha = \beta = \gamma = 90°$
Monoclinic	$a \neq b \neq c$	$\alpha = \gamma = 90° \neq \beta$
Triclinic	$a \neq b \neq c$	$\alpha \neq \beta \neq \gamma \neq 90°$

Experimental determination of a crystal's space group is carried out using diffraction techniques, such as x-ray or neutron diffraction. The International Tables for X-Ray Crystallography contain information on the symmetry operations assocatied with each space group, and detailed symmetry analysis of specific materials are found in the

series of books from R.W.G. Wyckoff. Information obtained from Wyckoff's books entails the number of allotropic structures, the space group designations of each structure, and the symmetries associated with each atom's position in a structure's primitive cell.

4. PHONONS

Having discussed the structure of crystal lattices, the following section describes the atomic vibrational modes, or phonons, of a lattice and their relationship with temperature. First, a basic 1D model of atomic vibrations is presented in order obtain the general characteristics of phonons. This is followed by an overview of a group theory-based method of determining the symmetry and number of phonon modes associated with a given primitive cell. Finally, the section concludes with a discussion on the temperature dependence of phonon energies.

4.1 Phonon Properties

The vibrational energy of a crystal lattice is quantized into quasi-particles known as phonons. Phonons communicate vibrational energy within a lattice. Phonons in the quasi-particle treatment are considered to be bosons and obey Bose-Einstein statistics, with the equilibrium population of phonons having frequency ω at temperature T being

$$n(\omega, T) = \frac{1}{\exp\left(\frac{\hbar c\omega}{k_B T}\right) - 1} \tag{7}$$

where h and k_B are the Planck and Boltzmann constants, respectively, and c is the speed of light. Equation 6 is known as the Bose function.[10] Approximating the confining potential of each atom to be harmonic, the energy of n phonons in a mode with frequency ω is given by

$$E_n = \left(n + \tfrac{1}{2}\right)\hbar\omega \tag{8}$$

4.2 1D-Diatomic Chain Model

A basic understanding of phonons in a polyatomic crystal is available through a simplified model consisting of a diatomic chain of atoms with masses m_1 and m_2.[9] Each diatomic pair is associated with an atomic plane with index *s* and thickness *a*, and the model is assumed to satisfy a specific set of boundary conditions known as Born-von Karman boundary conditions (Fig. 2).

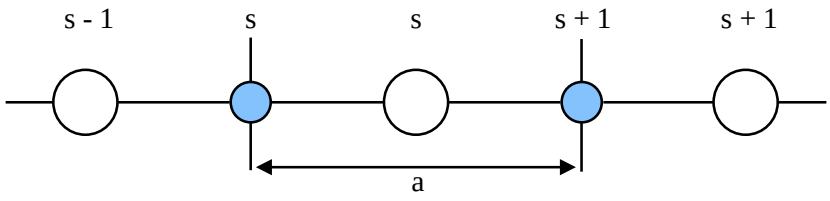

Figure 2: 1D-Plane Model of a Diatomic Chain. The indices of each diatomic plane are indicated above the atoms.

Assuming a linear restoring force between atoms, and separately considering the displacement of each atom from equilibrium, two coupled differential equations of motion, one per specie, are constructed:

$$m_1 \frac{d^2 u_s}{dt^2} = C[v_s + v_{s-1} - 2u_s] \tag{9}$$

$$m_2 \frac{d^2 v_s}{dt^2} = C[u_{s+1} + u_s - 2v_s] \tag{10}$$

where u_s and v_s represent the off-equilibrium displacements of atoms in plane *s* with masses m_1 and m_2 (respectively). Assuming plane wave solutions of

$$u_s = ue^{i(ska-\omega t)} \tag{11}$$

$$v_s = ve^{i(ska-\omega t)} \tag{12}$$

and inserting Eq. (3) and Eq. (4) into Eq. (1) and Eq. (2) yields

$$-\omega^2 m_1 u = Cv\left[1 + e^{-ika}\right] - 2Cu \tag{13}$$

$$-\omega^2 m_2 v = Cu\left[e^{ika} + 1\right] - 2Cv \tag{14}$$

The dispersion relation *ω(k)* is found by solving the characteristic equation of the coupled differential equations. Equating the following determinant of the matrix constructed from Eq. (13) and (14) to zero yields the characteristic equation:

$$\begin{vmatrix} 2C - m_1\omega^2 & -C(1 + e^{-ika}) \\ -C\left(1 + e^{ika}\right) & 2C - m_2\omega^2 \end{vmatrix} = 0 \tag{15}$$

$$\Longrightarrow 4C^2 - 2C(m_1 + m_2)\omega^2 + m_1 m_2 \omega^4 - C^2\left(1 + e^{ika}\right)\left(1 + e^{-ika}\right) = 0 \tag{16}$$

Rewriting the last term as $2 + 2\cos(ka)$ to simplify the expression yields a characteristic equation that is quadratic in ω^2. Furthermore, the long wavelength limit of $k \to 0$ is obtained using the expansion $\cos(ka) \simeq 1 - {}^1\!/_2\, k^2a^2$ for small *k*:

$$\Rightarrow m_1 m_2 \omega^4 - 2C(m + m)\omega^2 + C^2 k^2 a^2 = 0 \tag{17}$$

Solving Eq. (9) for ω^2 and taking the square root of the solution arrives at the sought after expression of *ω(k)*.

$$\Longrightarrow \omega^2 = \frac{2C(m_1 + m_2) \pm \sqrt{4C^2(m_1 + m_2)^2 - 4m_1 m_2 C^2 k^2 a^2}}{2m_1 m_2} \tag{18}$$

At k=0, the long wavelength solutions of Eq. (10) are

$$\omega_1{}^2 = 0\ acoustic \tag{19}$$

$$\omega_1{}^2 = 2C\left(\frac{m_1 + m_2}{m_1 m_2}\right) = 2C\left(\frac{1}{m_1} + \frac{1}{m_2}\right)\ optical \tag{20}$$

At the zone boundary $k = \pm\frac{\pi}{a}$, and Eq. (16) becomes

$$\omega^4 m_1 m_2 - 2C(m_1 + m_2)\omega^2 + 4C^2 = 0 \tag{21a}$$

$$\omega^4 - 2C\left(\frac{1}{m} + \frac{1}{m}\right)\omega^2 + \frac{4C^2}{m_1 m_2} = 0 \tag{21b}$$

$$\Longrightarrow {\omega_1}^2 = \frac{2C}{m_1}\ (acoustic\ ), \qquad {\omega_2}^2 = \frac{2C}{m_2}\ (optical) \tag{22}$$

Assuming m_1 is greater than m_2 implies ${\omega_1}^2 < {\omega_2}^2$, and a plot of *ω(k)* in the first Brillouin zone reveals the seperate acoustic and optical phonon branches:

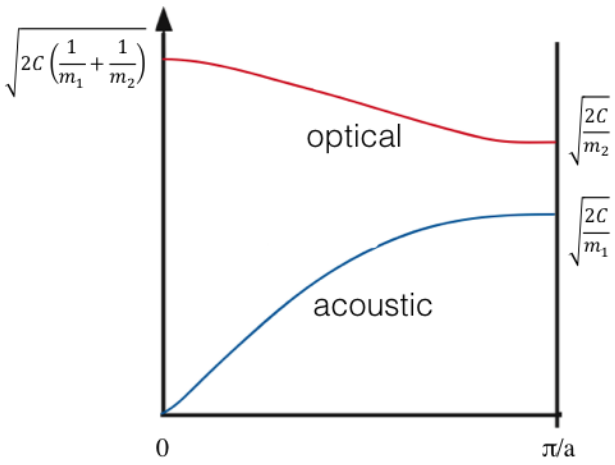

Figure 3: Acoustic and Optical Phonon Branches.

Solutions of ω(*k*) occurring between the branches correspond to a complex wavevector. Inserting complex *k* values into the plane wave solutions given by Eq. (10) and Eq. (11) yield exponentially decaying amplitudes. The dampening of waves with frequencies occurring between the branch gap at the zone boundary is a characteristic feature of polyatomic lattices.[9]

The motion of the atomic species is different for the acoustic and optical modes in the long wavelength limit ($k \to 0$). In analogy to acoustic waves in a gas, acoustic modes

consist of neighboring atoms oscillating in phase.[14] For an optical mode, the center of mass is motionless relative to the crystal and neighboring atoms oscillate with opposing phase. Substituting ω^2 into Eq. (12) and (13) and solving for the ratio of the amplitudes yields this behavior mathematically

$$\frac{u}{v} = -\frac{m_2}{m_1} \tag{23}$$

In three dimensional space, there are 3N vibrational modes for a primitive cell containing N atoms. Three of these modes are associated with acoustical phonon modes, which means a total of 3N-3 optical phonon modes exist. The atomic displacements of optical phonon mode are categorized as either being longitudinal or transverse. In a longitudinal optical (LO) phonon the atomic displacements are in parallel with the wavevector of the phonon. The atomic displacements in a transverse optical (TO) phonon mode are perpendicular to the wavevector of the phonon.

A lattice vibration is characterized by its frequency ω and its wavevector k. Since k is a representation of relative coordinates, it is not related to physical momentum. The physical momentum of a phonon in this model is given by

$$p = M\frac{d}{dt}\left(\sum_s u_s(t)\right) \tag{24}$$

where, for N atoms, s=0, ⋯, N-1

$$= M\frac{d}{dt}\left(\sum_s u e^{i(ska-\omega t)}\right) \tag{25}$$

$$= M(-i\omega t u)\sum_s e^{i(ska-\omega t)} \tag{26}$$

For Born-von Karman boundary conditions, which are boundary conditions used to model crystal structur, the values of k are $k = \frac{2\pi m}{Na}$, with $m = 0, 1, \cdots$. Using the series formula of

$$\sum_{1}^{N} x^s = \frac{1 - x^N}{1 - x} \tag{27}$$

and letting $x = e^{i(ka - \omega t)}$ yields an expression for phonon momentum of

$$p = M\left(-i\omega e^{-i\omega t}\right)\left(\frac{1 - e^{iN\left(\frac{2\pi m}{Na}\right)a}}{1 - e^{i\left(\frac{2\pi m}{Na}\right)a}}\right). \tag{28}$$

From the argument of the numerator in Eq. (28), it is concluded that

$$\Longrightarrow p = 0\,.$$

Thus, phonons are not associated with a physical momentum, but instead carry *crystal momentum* $\hbar k$.[9] A discussion on how phonons behave in their interactions with other particles will be brought forth in section 5.

4.5 Thermal Effects

Increasing the temperature of a crystal causes a decrease in phonon frequency. The decrease of phonon frequency with temperature is referred to as phonon redshift and the temperature dependent redshift can be expressed as

$$\omega(T) = \omega_0 + \Delta_1(T) + \Delta_2(T) \tag{29}$$

where ω_0 is the harmonic frequency of the phonon mode at low temperature, $\Delta_1(T)$ is the thermal expansion contribution, and $\Delta_2(T)$ corresponds to effects of anharmonic phonon decay.[12]

The expression describing the temperature dependence of phonon energy (Eq. 29) can be obtained by explicitly considering the primitive cell volume V in the derivative of ω with respect to T

$$\frac{d\omega}{dT} = \frac{\partial\omega}{\partial V}\frac{\partial V}{\partial T} + \left.\frac{\partial\omega}{\partial T}\right|_V. \tag{30}$$

In Eq. 30, the derivative containing $\frac{\partial\omega}{\partial V}$ can be expressed in terms of the Grüneisen parameter γ, which describes how phonon frequency is affected by changes in primitive cell volume

$$\frac{\partial\omega}{\partial V} = -\gamma\frac{\omega_0}{V}. \tag{31}$$

Substituting $\frac{\partial\omega}{\partial V}$ in terms of γ into Eq. 30 and then integrating with respect to temperature yields

$$\omega(T) = \omega_0 - \gamma\omega_0\int_0^T \frac{1}{V}\frac{\partial V}{\partial T'}\,dT' + \int_0^T \left.\frac{\partial\omega}{\partial T'}\right|_V dT'. \tag{32}$$

Comparing Eq. 32 with Eq. 29, the first integral term containing γ is the thermal expansion contribution to redshift $\Delta_1(T)$, and the second integral term represents the effects of anharmonic phonon decay $\Delta_2(T)$.

For uniaxial crystals, which have only two unique lattice constants a and c, the volume of the primitive cell can be approximated as $V = a^2c$. Using this approximated volume, the logarithmic derivative of volume found in the first integral of Eq. 32 becomes

$$\frac{1}{V}\frac{\partial V}{\partial T} \approx \frac{1}{c}\frac{\partial c}{\partial T} + \frac{2}{a}\frac{\partial a}{\partial T}, \tag{33}$$

where $\frac{1}{c}\frac{\partial c}{\partial T}$ and $\frac{1}{a}\frac{\partial a}{\partial T}$ are the temperature dependent linear thermal expansion coefficients parallel and perpendicular to the c axis, denoted by $\alpha_c(T)$ and $\alpha_a(T)$. The coefficients are expressed in dimensions of [1/temperature]. Now, the thermal expansion contribution to redshift found in Eq. 29 is given by[12]

$$\Delta_1(T) = -\omega_0 \gamma \int_{T'=0}^{T} [\alpha_c(T') + 2\alpha_a(T')] dT' \,. \tag{34}$$

The linear thermal expansion coefficients are provided for a uniaxial crystal because the material studied in this work, 6H-SiC, is hexagonal. The properties of the sample are further described in the Experimental section.

Anharmonic phonon decay occurs when a phonon decays into two or more lower energy phonons, given that both total energy and wavevector are conserved according to

$$\omega = \sum_{i=1}^{N} \omega_i \tag{35}$$

$$\boldsymbol{q} = \sum_{i=1}^{N} \boldsymbol{q_i} + \boldsymbol{G} \tag{36}$$

respectively, where ω represents the initial phonon energy and ω_i represents the created phonon energy (in cm^{-1}), and **G** is the reciprocal lattice vector.[13]

The decay related broadening of phonon energies can be understood using the single-mode relaxation approach. In this approach, the initial zone-centered phonon has a non-equililbrium population which arises from the Raman process described in section 5. All other phonons are assumed to have an equilibrium population. In the single-mode relaxation approach the decay related broadening is given by[13]

$$\Gamma(\mathbf{0}, j; \omega) = \frac{18\pi}{\hbar^2} \sum_{\boldsymbol{q}, j_1, j_2} |V_3|^2 \times \left[n_{j_1}(\boldsymbol{q}) + n_{j_2}(-\boldsymbol{q}) + 1\right] \times \delta\left[\omega(\mathbf{0}) - \omega_{j_1}(\boldsymbol{q}) - \omega_{j_2}(-\boldsymbol{q})\right] \tag{37}$$

$$+ \frac{96\pi}{\hbar^2} \sum_{\boldsymbol{q}_1, \boldsymbol{q}_2, \boldsymbol{q}_3, j_1, j_2, j_3} |V_4|^2$$

$$\times \left\{\left[n_{j_1}(\boldsymbol{q}_1) + 1\right]\left[n_{j_2}(\boldsymbol{q}_2) + 1\right]\left[n_{j_3}(\boldsymbol{q}_3) + 1\right]\right.$$

$$\left. - n_{j_1}(\boldsymbol{q}_1) n_{j_2}(\boldsymbol{q}_2) n_{j_3}(\boldsymbol{q}_3)\right\}$$

$$\times \delta\left[\omega(\mathbf{0}) - \omega_{j_1}(\boldsymbol{q}_1) - \omega_{j_2}(\boldsymbol{q}_2) - \omega_{j_3}(\boldsymbol{q}_3)\right].$$

In Eq. (37), the Dirac δ appearing in each term comes from the phonon density of states arguments. It ensures the conservation of energy (explicit) and wavevector (implicit) in the allowed transitions. The first summation originates from the anharmonic factor of the vibrational Hamiltonian and describes the decay of one zone-centered phonon into two phonons with opposite wavevectors. The second summation originates from the fourth order expansion factor in the vibrational Hamiltonian and corresponds to the decay of one zone-centered phonon into three phonons under the constraint $\boldsymbol{q}_1 + \boldsymbol{q}_2 + \boldsymbol{q}_3 = 0$. The matrix elements V_3 and V_4 are related to the Fourier transformed cubic and quadratic anharmonic force constants.[13]

The phonon energy shift resulting solely from anharmonic decay can be expressed through the Kramers-Kronig transform of Eq. (33),

$$\Delta(\mathbf{0}, j, \omega) = -\frac{2}{\pi} P \int_0^\infty \frac{\omega' \Gamma(\mathbf{0}, j, \omega)}{(\omega'^2 - \omega^2)} d\omega' \tag{38}$$

where P denotes the principal part of the integral.[13]

The situation described in each term of Eq. (37) involves a phonon decaying into only a few vibrations with in the BZ. When two- and three-phonon decay processes can be attributed to a single or narrow set of created phonons, each summation in Eq. (37) may be replaced by a single term. Furthermore, the coefficients of the two- and three-phonon decay processes in Eq. (38) may be represented by simplified parameters A and B. This simplification allows us to express the phonon decay contribution to redshift appearing in Eq. (29) as

$$\Delta_2(T) = -A[1 + n(\omega_1, T) + n(\omega_2, T)] \qquad (39)$$
$$- B[1 + n(\omega_3, T) + n(\omega_4, T) + n(\omega_5, T) + n^2(\omega_3, T) + n^2(\omega_4, T)$$
$$+ n^2(\omega_5, T)]\,,$$

where $n(\omega, T)$ is the Bose function at energy $hc\omega$, with ω expressed in cm^{-1}.[13] The first term of $\Delta_2(T)$ represents a two-phonon decay process in which ω decays into two phonons with energies ω_1 and ω_2. The second term corresponds to a three-phonon decay process in which ω decays into phonons with energies ω_1, ω_2, and ω_3. The parameters A and B represent the relative probabilities of each decay process and are commonly treated as fitting parameters.[12]

The most relevant anharmonic decay mechanism for the E_2(TO) phonon, which is the mode of 6H-SiC studied in this work, is known as the Klemens process. The Klemens process refers to when an optical phonon decays into two identical acoustic phonons with opposite momenta.[13] The experimental verification of this is described in section 7.

In crystals, Raman linewidths (Γ) are inversely proportional to the overall phonon lifetime (τ_{total}), which is influenced by anharmonic decay and by impurity and defect scattering

$$2\pi c\Gamma = \frac{1}{\tau_{total}} = \frac{1}{\tau_{decay}} + \frac{1}{\tau_i} \tag{40}$$

where c is the speed of light in vacuum in cm/s, Γ is in cm^{-1}, τ_{decay} is the average phonon decay time, and τ_i represents the effect of all impurity and defect related phonon scattering.[13] In a high-quality crystal the amount of impurities and defects is negligible and the phonon lifetime appropriately represents the phonon decay time. Therefore, Raman peak width measurements yield the average phonon decay time. The Raman effect is discussed in section 5.

The effects of temperature on phonon lifetime are described by

$$\Gamma(T) = \Gamma_0 + \Delta_2'(T) \tag{41}$$

where $\Delta_2'(T)$ is identical in form to expression $\Delta_2(T)$ but with A and B replaced by the parameters C and D. The parameters C and D are associated with the relative importance of phonon-phonon interactions and are treated as fitting parameters.[12]

5. THE RAMAN EFFECT

For monochromatic light incident upon a crystal, the majority of scattered photons have the same energy as the incident light, $\hbar\omega_I$. However, approximately 1 in 10^7 incident photons inelastically scatter from the crystal with energies differing from $\hbar\omega_I$. The inelastic scattering of light is known as the Raman effect and is named after the prominent Indian physicist C.V. Raman, who discovered the effect in 1923. Raman spectroscopy is the study of the interaction of light with molecular and crystal vibrations. Raman spectroscopy has become an integral part of material science and its applicability has substantially increased since the recent advent and commercialization of CCDs, solid-state lasers, and other optoelectronic technologies.[14]

5.1 Classical Definition

The inelastic scattering of light can be understood macroscopically using classical electrodynamics. Assuming a coherent and monochromatic source of incident light, dipoles are induced in the scattering medium by the electric field of the incident light. Mathematically, this is expressed as

$$\boldsymbol{P} = \epsilon_o \chi \boldsymbol{E} \tag{42}$$

where $\boldsymbol{P}$ is the polarization and χ is the electric susceptibility.[15] Let Q_s denote a normal coordinate of the excited phonon mode which has frequency ω_s and a time dependence of

$$Q_s(t) = Q_s^0 \cos(\omega_s t)\ . \tag{43}$$

In terms of the normal coordinates for nuclei positions, the expanded form of χ to first order is given by

$$\chi(t) = \left(\chi_{jl}\right)_0 + \sum_s \left(\frac{\partial \chi_{jl}}{\partial Q_s}\right)_0 Q_s + \cdots \tag{44}$$

$$\approx \left(\chi_{jl}\right)_0 + \sum_s \left(\frac{\partial \chi_{jl}}{\partial Q_s}\right)_0 Q_s^0 \cos(\omega_s t)\,. \tag{45}$$

For incident light with frequency ω_I and a time dependent electric field of

$$\boldsymbol{E}(t) = \boldsymbol{E}_0 \cos(\omega_I t)\,, \tag{46}$$

the expression for polarization becomes

$$\boldsymbol{P}(t) = \epsilon_o \left[\left(\chi_{jl}\right)_0 + \sum_s \left(\frac{\partial \chi_{jl}}{\partial Q_s}\right)_0 Q_s^0 \cos(\omega_s t)\right] \boldsymbol{E}_0 \cos(\omega_I t) \tag{47}$$

$$= \epsilon_o \left(\chi_{jl}\right)_0 \boldsymbol{E_0} \cos(\omega_I t) + \sum_s \left(\frac{\partial \chi_{jl}}{\partial Q_s}\right)_0 Q_k^0 \boldsymbol{E}_0 \cos(\omega_s t)\cos(\omega_I t) \tag{48}$$

$$= \epsilon_o \left(\chi_{jl}\right)_0 \boldsymbol{E}_0 \cos(\omega_I t) \tag{49}$$

$$+ \sum_s \left(\frac{\partial \chi_{jl}}{\partial Q_s}\right)_0 Q_s^0 \boldsymbol{E}_0 \left\{\tfrac{1}{2}\left[\cos\left((\omega_I + \omega_s)t\right) + \cos\left((\omega_I - \omega_s)t\right)\right]\right\}.$$

The first term in the expression is the polarization component that radiates the elastically scattered light. The second term represents the polarization component which radiates inealstically scattered light, and does so at two frequencies: ω_I that is upward modulated by ω_s, and ω_I which is downward modulated by ω_s.[16]

The summation in the second term is known as the Raman tensor. It is a symmetric tensor and its components are known as susceptibility derivatives.[14] Each Raman tensor component is associated with three indices. The indices *j* and *l* extend over the Cartesian coordinates from 1 to 3 and index *s* runs over the 3N-3 normal coordinates of the phonon modes with wavevector $\boldsymbol{k} = 0$, where N is defined to be the number of atoms per primitive cell.[16]

5.2 Momentum and Energy Conservation

Photons that scatter with energies less than $\hbar\omega_I$ are referred to as the Stokes component of the scattered intensity, and photons scattering with energies greater than $\hbar\omega_I$ are known as the anti-Stokes component (Fig. 4).[14]

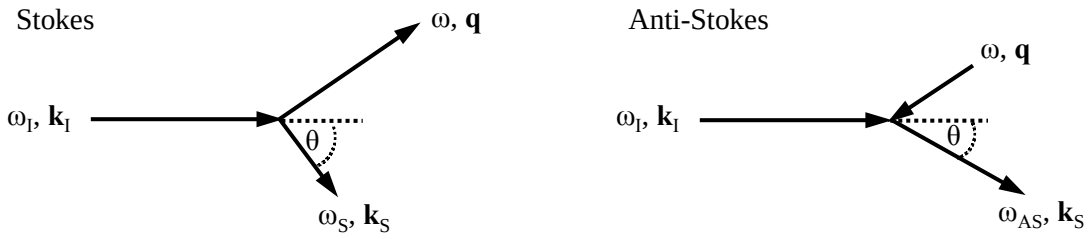

Figure 4: Stokes and Anti-Stokes Scattering Events. Momentum changes associated with a Stokes and anti-Stokes scattering event.

The conservation of energy and momentum dictate that in a Stokes scattering event the incident photon transfers energy $\hbar\omega$ and momentum $\boldsymbol{k}$ to the medium, where

$$\omega = \omega_I - \omega_S \,, \tag{50}$$

$$\boldsymbol{k} = \boldsymbol{k_I} - \boldsymbol{k_S} + \boldsymbol{G} \,. \tag{51}$$

In an anti-Stokes event the medium transfers energy $\hbar\omega'$ and momentum $\boldsymbol{k}'$to the scattered photon, where

$$\omega = \omega_{AS} - \omega_I \,, \tag{52}$$

$$\boldsymbol{k}' = \boldsymbol{k_{AS}} - \boldsymbol{k_I} + \boldsymbol{G} \,. \tag{53}$$

The subscripts I, S, and AS indicate the incident, Stokes and anti-Stokes photons (respectively), and **G** is the reciprocal lattice vector (Fig. 4).[14]

The Stokes component of scattered intensity corresponds to the generation of excitations in the crystal structure, whereas the anti-Stokes component corresponds to their annihilation.[14] The upward and downward modulations of energy exhibited by the inelastically scattered light are referred to as Raman shift. At room temperature, the population of phonons generated by Stokes scattering exceeds the population of phonons annihilating in anti-Stokes scattering. Hence, most Raman scattering experiments measure the Stokes component on account of its greater intensity.

From Eq. (50), the wavelength of the scattered light is given by

$$\lambda_s = \frac{1}{\bar{\nu}_I - \bar{\nu}} \,, \tag{54}$$

where $\bar{\nu}_I$ is the of the inverse of the incident light's wavelength and $\bar{\nu}$ is the Raman shift of the phonon. Raman shift are typically expressed in units of cm^{-1}, where 1 cm^{-1} = 0.1239 meV.

Lattice constants are typically on the order of a few Å, while the wavelength of visible light is on the order of 10^3Å. This three order of magnitude difference places the

wavevector of the incident photon near the center of the Brillouin zone. From this, the conservation of momentum indicates that only phonons found near the center of the Brillouin zone take part in the inelastic scattering of visible light.[10]

5.3 Microscopic Description of Stokes Scattering

Microscopically, the Stokes scattering of visible light in a semiconductor at non-zero temperatures can be described in three steps. The steps involve the states of the incident and scattered photons, the electrons of the semiconductor, and the phonons induced by scattering. Prior to the scattering event, the semiconductor is assumed to have an empty conduction band and a valence band that is completely filled with electrons. The electrons involved in scattering undergo virtual transitions and are left unchanged after the process, which conserves wavevectors but not necessarily energy.

In the first step, the semiconductor is excited from initial state $|i\rangle$ to an intermediate state $|a\rangle$ when an incident photon creates an electron-hole pair (exciton). Visible photons couple to electrons via the electron-radiation Hamiltonian $\widehat{H}_{eR}$,

$$\widehat{H}_{eR} = \frac{e}{mc}\vec{A} \circ \hat{p}\ , \tag{55}$$

where $\vec{A}$ is the vector potential in the Coulomb gauge and $\hat{p}$ is the momentum operator $(-i\hbar\nabla)$. The electrons of the semiconductor are assumed to have Bloch wavefunctions. A semi-classical approach is used to describe the interaction between electrons and the electromagnetic field, which is evident from the vector potential $\vec{A}$ found in $\widehat{H}_{e-Ion}$.

Next, the electron-hole pair scatters into a different intermediate state $|b\rangle$ by the emission of a phonon. The emission of a phonon involves the electron's interaction with the lattice ions through the electron-ion Hamiltonian $\widehat{H}_{e-Ion}$.

In the last step of the scattering process, the electron-hole pair described in state $|b\rangle$ emits a scattered photon upon radiative recombination via $\widehat{H}_{eR}$. This event leaves the semiconductor in state $|f\rangle$ with a pre-scattering band population, and so $|f\rangle = |i\rangle$. Furthermore, the last step is known as stimulated emission due to the necessity of the presence of an electromagnetic wave before the radiative recombination occurs.

In the microscopic picture of Raman scattering, the probability of the previously mentioned scattering process, P_{ph}, can be described via the Fermi Golden Rule

$$P_{ph}(\omega_s) = \frac{2\pi}{\hbar}\left|\sum_{n,n'} \frac{\langle i|\widehat{H}_{eR}|n'\rangle\langle n'|\widehat{H}_{e-ion}|n\rangle\langle n|\widehat{H}_{eR}|i\rangle}{[\hbar\omega_\iota - (E_n - E_i)][\hbar\omega_\iota - \hbar\omega_0 - (E_{n'} - E_i)]}\right|^2 \times \delta[\hbar\omega_\iota - \hbar\omega_0 - \hbar\omega_s]\,, \tag{56}$$

where $\hbar\omega_s$ is the energy of the phonon generated in the scattering process.

5.3 Basic Equipment

Setups designed to perform Raman spectroscopy usually contain several components. A laser provides a source of coherent, monochromatic light and optical elements, such as lenses and mirrors, are used to direct the laser to the sample and collect

the scattered light. A dispersive element is used to produce a spectrum of the scattered light and a detector is needed to record a portion of the spectrum.

6. EXPERIMENT

Achieving the main goal of observing in-situ sample holder temperatures required an initial calibration measurement of 6H-SiC's temperature dependent Raman shifts, as well as the construction of an apparatus which could obtain Raman spectra at the distance required for MBE chamber measurements.

Calibration measurements of 6H-SiC were performed on an optical table using a hot plate and thermocouple. Then, a macro-Raman apparatus was developed and tested in a laboratory setting until its range of detection sufficed for MBE measurements (Fig. 5). With the previous benchmark passed, the macro-Raman apparatus was rebuilt on site at the MBE growth chamber and in-situ 6H-SiC measurements were taken. Initial in-situ calibration measurements were performed using known temperatures, and then the technique was applied to a standard temperature ramp process.

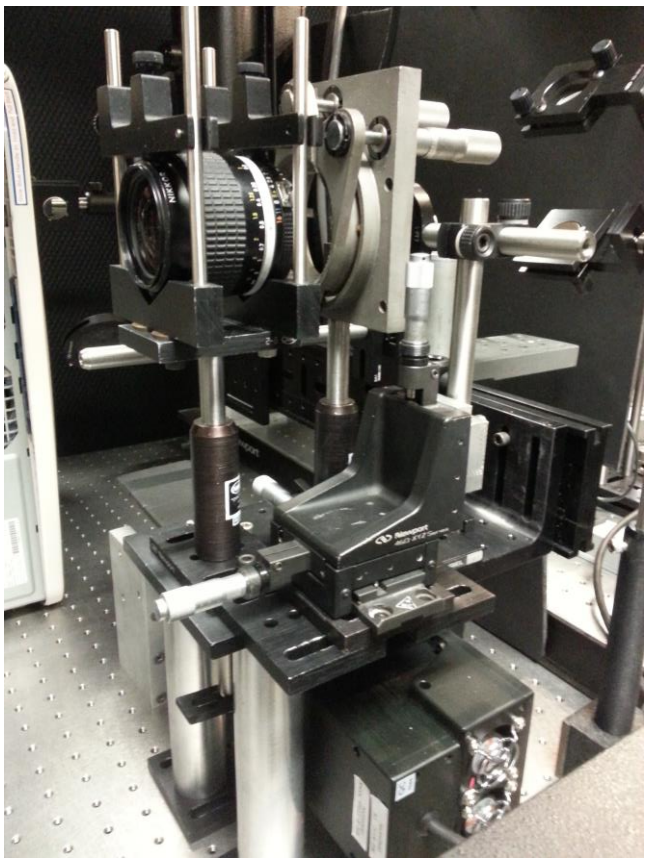

Figure 5: Prototype Macro-Raman Apparatus.

6.1 6H-SiC

A small piece ~ 1 cm^2 of a commercial 6H-SiC wafer (0.3 mm in thickness) was used as the substrate for the calibration and MBE measurements. Silicon carbide was chosen due to its robustness in the temperature range of interest and the availability of distinct Raman-active phonons. Silicon carbide is a ceramic semiconductor and has been identified to exist in more than 200 different polytypes.[17] A bilayer consisting of silicon and carbon atoms forms the basic building block of each SiC polytype. The 6H polytype belongs to the hexagonal crystal system and has a primitive cell that contains 6 bilayers arranged in a hexagonal structure (Fig. 6).

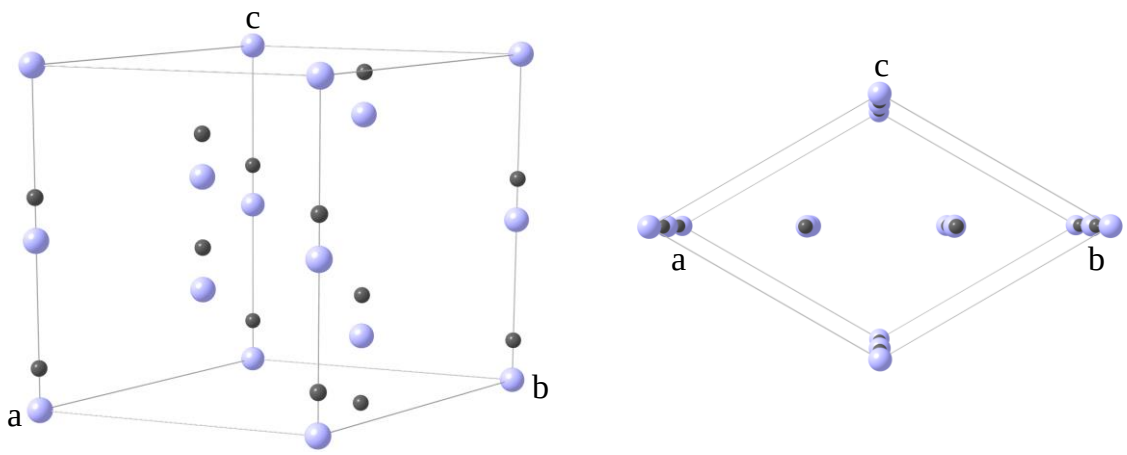

Figure 6: 6H-SiC Primitive Cell. The light-blue spheres represent Si atoms, the black spheres represent C atoms, and each sphere is approximately 1/3 of the actual atomic radii. The letters indicate the crystal axes.

The 6H polytype belongs to the C_{6v} crystallographic point group,[16] and the Raman active phonon modes of 6H-SiC occur with 3 different symmetries. Literature indicates there are Raman active phonon modes with A_1, E_1, and E_2 symmetries observable in a back scattering geometry along the c-axis.[16,18] The effect of temperature on phonon energy for 6H-SiC has been previously investigated[12,18] and 6H-SiC Raman peaks exhibit a temperature dependence as described in section 4.5 and shown in Fig. 7.

Shifts are attributed to thermal expansion and the effect of phonon decay as described in section 4.5. For the zone-center E_2 vibration, a symmetric two-phonon decay has been applied to adequately describe the dependence from 20–350 K.[12] Measurements of the Grüneisen parameter for 6H-SiC report a value[19] of $\gamma = 1.23$ and the coefficients of thermal expansion for the a- and c- crystal axes have been reported to be given by

$$\alpha_c(T) = 3.27 \times 10^{-6} + (3.25 \times 10^{-9})T - (1.36 \times 10^{-12})T^2 \,, \qquad (57)$$

$$\alpha_a(T) = 3.18 \times 10^{-6} + (2.48 \times 10^{-9})T - (8.51 \times 10^{-13})T^2 \,, \qquad (58)$$

where T is in °C and α_c and α_a are in $(°C)^{-1}$. [20]

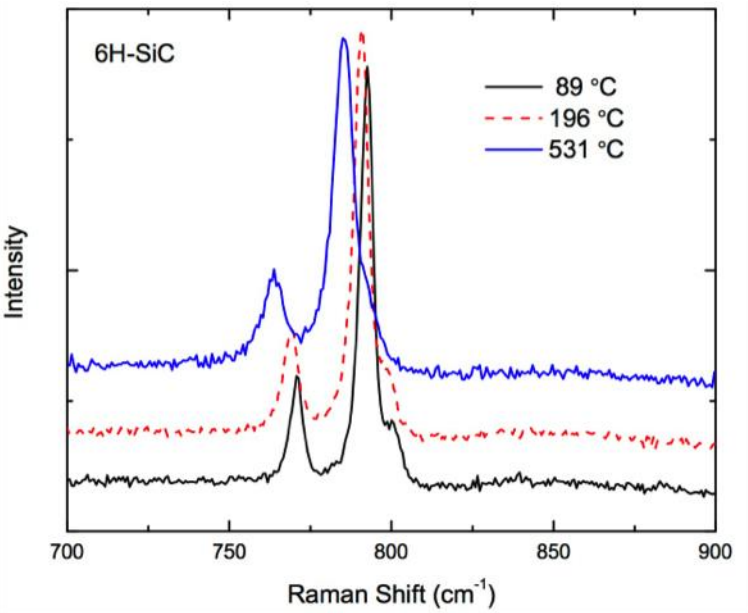

Figure 7: 6H-SiC Phonon Redshift. Redshift of phonon peaks in the Raman spectra of 6H-SiC at 89 °C, 186 °C, and 531 °C. The E_2 phonon peak is the most prominent peak displayed in the spectra.

6.2 Spectral Analysis

The spectral acquisition program WinSpec/32 managed CCD operations, parameter adjustments, and recorded unfitted spectra in the format of photon counts versus relative wavenumbers. The primary WinSpec/32 features used for both calibration and MBE measurements were setting CCD acquisition times, establishing CCD calibration, and converting spectra into ASCII formatted text files to be used in subsequent fitting procedures. Raman peak centers were obtained from the ASCII text

files using the program PeakFit, which carried out baseline subtraction and applied fits to peaks in each spectrum.

6.3 CCD Calibration

Prior to measuring 6H-SiC's temperature dependent Raman shift, the CCD chip must be calibrated to obtain spectrally accurate data. Correlating the wavelengths from a standard neon pen lamp with the pixels registering the peaks of the lamp's wavelengths allowed the Raman peaks of a 6H-SiC spectrum to be expressed in terms of wavenumbers. This was accomplished by placing the neon pen lamp in line with the spectrograph's entrance slit, at a distance of approximately 30 cm. The slit was set to a width of 10 μm and a 1 second CCD exposure was acquired. Then, in WinSpec/32, seven to ten wavelengths from neon's emission spectrum were paired with their peak center's pixel number. The wavelength of the laser was included in the assignment procedure so that Raman peaks could be expressed in terms of relative wavenumbers.

Selecting the correct set of calibrating wavelengths from a standard source, such as neon, entails using Eq. (54) and the laser's wavelength and Raman shift values to calculate the wavelengths of scattered light Then, the spectrometer's diffraction grating is rotated such that a CCD acquisition displays calibration wavelengths that encompass the scattered light's wavelengths of interest. For example, 532 nm laser light exciting a phonon mode with a Raman shift of 790 cm^{-1} produces scattered light with a wavelength of approximately 555 nm. Therefore, rotating the diffraction grating such that an

acquisition displays the neon emission peaks of 566.255 nm and 543.365 nm will permit the observation of a Raman peak at 790 cm^{-1}.

6.4 Laboratory Calibration Measurements

6.4.1 Setup

Initial measurements of 6H-SiC's temperature dependent Raman shift were performed on a standard optical table using the set-up shown in Fig. 8. A vertically oriented hot plate supplied heat to the sample of 6H-SiC described in section 6.1. Temperature readings were provided by a type-K thermocouple placed in contact with the crystal's surface and its terminals were cold-junction compensated by a 100 Ω thermistor. Two HP 34401 multimeters measured thermocouple voltage and thermistor resistance. The 514.5 nm line of an Innova 300 argon ion laser provided a source of monochromatic light and Raman spectra were obtained using a 0.5 m SPEX 500M Czerny-Turner spectrograph. The SPEX 500M was equipped with an 1800 g/mm grating with maximum throughput (blaze) at 500 nm. Spectrally dispersed light was detected using a liquid nitrogen cooled EEV 400x1340B CCD chip and an ST-133 controller from Princeton Instruments. CCD operations were managed by a PC running the spectral analysis software WinSpec/32.

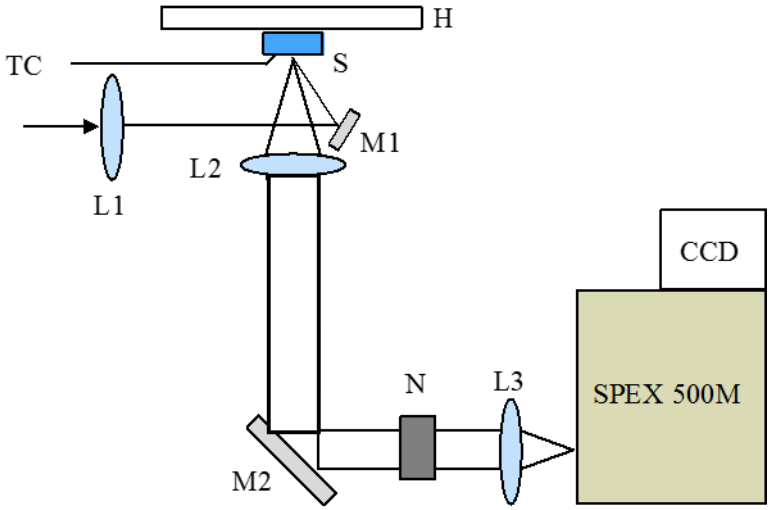

Figure 8: Laboratory Setup. Layout of laboratory setup used for calibrating the phonon energy redshift of 6H-SiC.

The optical path described by Fig. 8 consists of three lenses, two mirrors, and a holographic notch filter which rejects the laser's wavelength. Mirror M1 guides the beam focused by lens L1 onto the sample S, which is fixed to a hot plate H and located at the focal length of lens L2. The scattered light collected by lens L2 is collimated and directed through a holographic notch filter N by mirror M2. The filtered, collimated beam is focused onto the entrance slit of the spectrometer by lens L3. Lens L1 had a focal length of 20 cm; lenses L2 and L3 had a focal length of 10 cm.

Orientating the hot plate such that its surface was perpendicular to the table created a level optical path between the collection optics and the spectrometer's entrance slit. The hot plate's vertical orientation required the sample holder to be parallel to the plate's surface in order to provide sufficient thermal contact. Also, the sample holder needed to expose enough of the crystal's surface to fit the approximately 2 mm beam spot and thermocouple tip. These requirements were met by constructing a slotted right angle

from a 1 mm-thick sheet of aluminum. Then, the sample holder was mounted at the end of a 12 mm diameter stainless steel rod and positioned against the surface of the hot plate and in-line with the incident beam (Fig. 9).

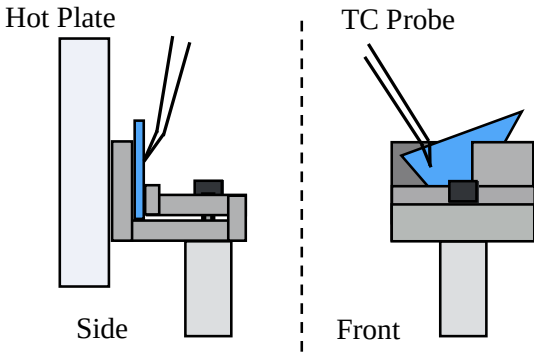

Figure 9: Sample Orientation for Calibration Measurements. The sample was positioned against the surface of the hot plate throughout calibration measurements. The thickness of the aluminum sheet is exaggerated to show detail.

6.4.2 Measurement Acquisition Sequence and Procedure

Simultaneous acquisitions of Raman spectra and thermocouple measurements were used to ensure that a consistent and repeatable calibration measurement process was performed at each setting of the hot plate's temperature controller. This was accomplished by simultaneously triggering measurement acquisition in each HP 34401 with a transitor-transitor-logic (TTL) signal from the ST-133 controller (Fig. 10). The controller outputs a TTL-high signal (4.5 V) from a BNC port when the CCD shutter is closed and a TTL-low (0 V) signal when the shutter is opened. Conveniently enough, the external trigger mode of the HP 34401 multimeter enables data acquisition when it receives a TTL-low signal.

The procedure for obtaining Raman spectra at different temperatures consisted of setting the hot plate's power level, waiting until the temperature stabilized, then initiating a 1 second CCD acquisition. The multimeters were set to acquire 100 thermistor and thermocouple measurements during the 1 second spectrum acquisition period.

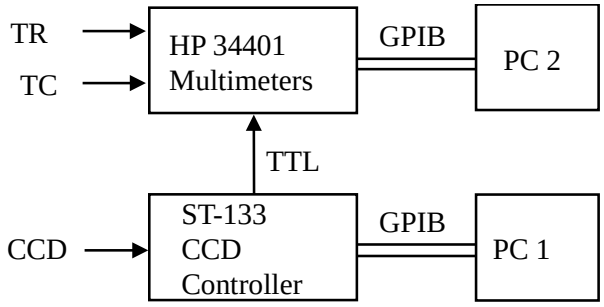

Figure 10: Temperature Measurement Acquisition Sequence. HP 34401 multimeters record thermistor (TR) and type-K thermocouple (TC) measurements upon receiving a TTL pulse from the CCD controller.

6.4.3 Temperature Data Conversion Process

Upon initiating a CCD acquisition with the computer labeled PC1, the multimeters sent thermocouple and thermistor data via GPIB to a second computer, PC2, where the raw data was logged and used to calculate an average temperature for the acquisition period. Data logging was performed by a LabView virtual instrument (VI). After each CCD acquisition, the VI produced a text file containing a 2D array of 100 voltage and resistance measurements. The thermistor and thermocouple measurements were averaged before being converted into a temperature value. In Microcoal Origin, the cold-junction-compensation process for each acquisition period began by converting the

thermistor resistance to temperature using the Steinhart-Hart equation.[21] The temperature of a thermistor is related to its resistance by

$$\frac{1}{T} = A + B[ln(R)] + C[\ln(R)]^3 , \tag{59}$$

where temperature T is in Kelvin and R is in Ohms. The constants A, B, and C are calculated using three established temperature-resistance data points of the particular thermistor and are provided by the manufacturer. For thermistor data points (T_1, R_1), (T_2, R_2), and (T_3, R_3) the constants are evaluated by first defining the following

$$Y_i = {T_i}^{-1} , \tag{60}$$

for $i = 1, 2, 3$, and

$$\gamma_2 = \frac{Y_2 - Y_1}{L_2 - L_1} , \qquad \gamma_3 = \frac{Y_3 - Y_1}{L_3 - L_1} . \tag{61}$$

Using the previously defined terms, the constants are given by

$$C = \left(\frac{\gamma_3 - \gamma_2}{L_3 - L_2}\right)(L_1 + L_2 + L_3)^{-1}, \tag{62}$$

$$B = \gamma_2 - C\left({L_1}^2 + L_1 L_2 + {L_2}^2\right) , \tag{63}$$

$$A = Y_1 - \left(B + {L_1}^2 C\right)L_1 . \tag{64}$$

Next, the thermistor temperature value was converted to a type-K thermocouple voltage using the type-K temperature dependent voltage equation

$$t_{90} = \sum_{i=0}^{n} b_i E^i . \tag{65}$$

The resulting value was added to the corresponding type-K thermocouple measurement dependent temperature equation

$$E = \sum_{i=0}^{n} c_i (t_{90})^i + \alpha_0 exp[\alpha_1 (t_{90} - 126.9686)^2] \,. \tag{66}$$

In both of the type-K thermocouple equations, E is the thermoelectric voltage in μV and t_{90} is temperature in degrees Celsius. The coefficients α_0, α_1, b_i, and c_i were taken from the NIST tables for the Type-K thermocouple.[22] Finally, the cold-junction compensated temperature from a single acquisition was associated with the corresponding E_2 phonon peak measurement. Conversion of the thermistor and thermocouple data indicated the laboratory calibration procedure yielded 15 data points occurring in approximately 10-15°C intervals over a range of room temperature to 162°C.

6.5 In-situ MBE Measurements

The sequence of measurements performed on the DCA M600 MBE chamber were carried out with a macro-Raman apparatus that was qualified in the laboratory and then reconstructed at the MBE site. The sequence of measurements consisted of an initial calibration using two known temperatures and then performing spectral acquisitions throughout a standard temperature ramp procedure.

6.5.1 Macro-Raman Apparatus

The excitation source was a solid-state Nd:YAG laser operating at 532 nm. Laser-focus and collection optics utilized a commercial camera objective capable of short working distances (35 cm). This objective focused the laser onto the sample with nominal spot diameter ~ 1 mm. The distance between the objective and sample in the MBE chamber was 45 cm for this demonstration. Scattered light collected by the camera objective was collimated, passed through a standard notch filter, and focused on the entrance slit of a the SPEX 500M spectrometer equipped with the same diffraction grating and CCD detector as described in section 6.4.1. Wavelength calibration was carried out using a standard neon pen lamp and the method described in section 6.3.

6.5.2 Setup

Temperature measurements of 6H-SiC were performed with the marco-Raman apparatus installed underneath a DCA M600 MBE growth chamber (Fig. 11 and Fig. 13). Optical access to the manipulator head was through a view port located approximately 45 cm underneath it. Scattered light was directed to the SPEX 500M spectrograph and CCD camera which was located approximately 2 m away from the view port. In the MBE chamber the sample is mounted to the molybdenum block using indium. The block is transferred into the chamber through a load-lock and held mechanically and thermally via a bayonet-style mount. The thermocouple is positioned on the opposite side of the molybdenum block from the sample, and not in physical (thermal) contact, as depicted in

Fig. 12. The manipulator head's temperature was controlled by software running on a computer located near the MBE growth chamber. The software provided temperature set points, ramp rates, and thermocouple readings.

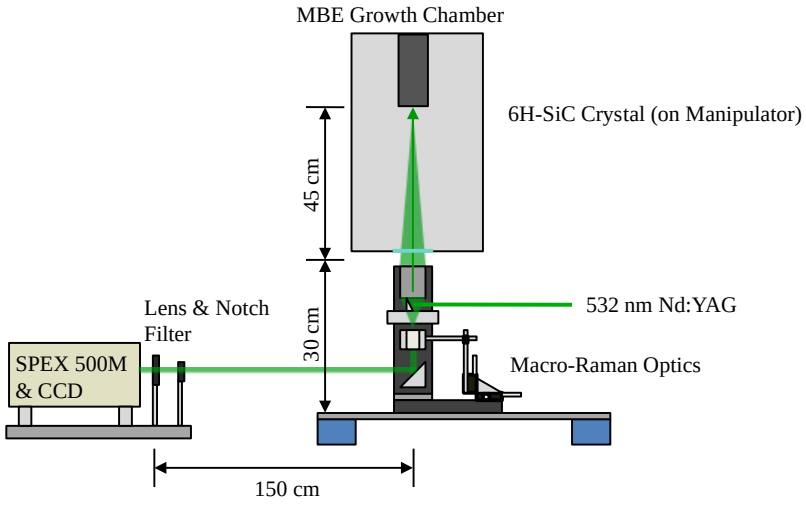

Figure 11: Macro-Raman MBE Layout. The dimensions specified in the illustration are representative of the dimensions encountered at the MBE site.

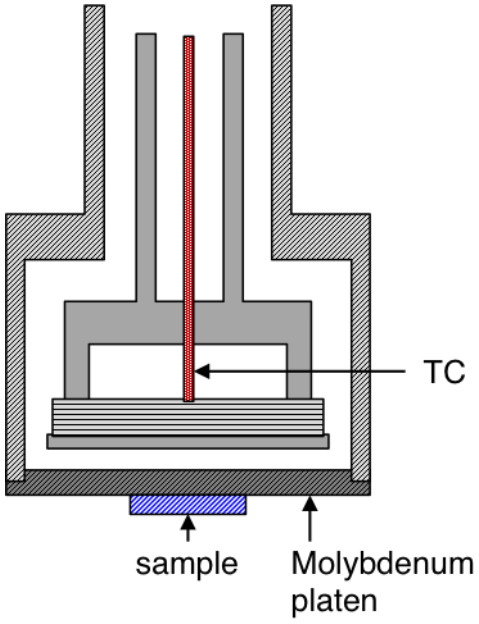

Figure 12: MBE Sample Manipulator.

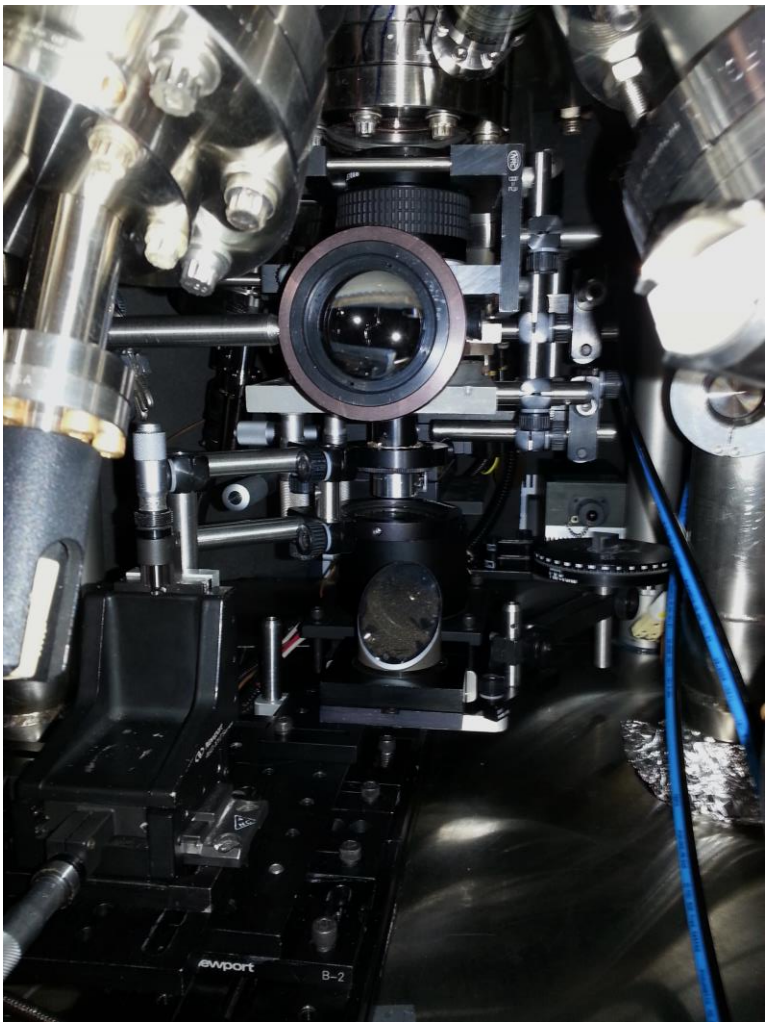

Figure 13: Macro-Raman Apparatus underneath MBE Growth Chamber.

6.5.3 Reference Temperature Measurement Procedure

Calibration of the Raman positions was accomplished by measuring 6H-SiC spectra at two independently known temperatures with the sample in place. The first temperature was the melting point of indium at 156.6 °C, the second was the melting point of InSb at 527 °C.[2,23] Both of these melting points were readily confirmed visually through another viewport and Raman spectra subsequently acquired at these known temperatures.

6.5.4 Standard Temperature Ramp Measurements

To illustrate the importance of absolute Raman temperature measurement to the standard thermocouple, measurements of a standard temperature ramp were carried out in the MBE chamber with the 6H-SiC sample affixed to the wafer chuck. The standard temperature ramp measurements consisted of performing a set of twenty-five acquisitions, each being 60 seconds in duration, as the temperature was ramped from 150 °C to 550 °C at a rate of 30 °C per minute. Measurements of the ramp process were performed with a growth chamber pressure of approximately 8.0×10^{-11} Torr, the spectrometer's slit width set to 80 μm, and less than a second delay between each acquisition in the second thermal profile.

7. RESULTS

7.1 Calibration Measurements

The E_2 phonon peak of 6H-SiC was chosen for fitting due to its prominence and was used to assess the calibration data and determine the unknown MBE temperatures. Spectra were fit with Lorentzian line shapes. Assuming a Klemens process for the anharmonic decay of the E_2 phonon yielded the best fit for the laboratory and MBE calibration data, where ω_1 and ω_2 were assumed to be $\frac{\omega_0}{2}$ in Eq. (29) through Eq. (41).

Fig. 14(a) depicts the calibration data. The phonon redshift predicted from thermal expansion alone is indicated by the red dashed curve, and the prediction of anharmonic phonon decay is given by the blue dashed curve. The black curve represents the predicted phonon shift when both effects are incorporated. Fitting the Raman spectra obtained from the calibration measurements yielded the parameters of ω_0 = 792.0 cm^{-1} and A = 3.0 cm^{-1} for the E_2 phonon peak. These values are both in good agreement with what has been previously reported.[12]

At the indium melting point of approximately 157 °C the value of the E_2 phonon peak center measured with the Nd:YAG's 532 nm laser line increased from the value obtained with the 514.531 nm line by 3.48 ± 0.18 cm^{-1}. This increase is attributed to the fact that the argon-ion laser line of 514.531 nm is known to a higher degree of accuracy than the Nd:YAG 532 nm laser line, which changes the relative wavenumber value of the phonon peak's center. Also, the offset includes any minor differences arising from the

Ne-calibration procedure, which would normally be quantifiable through comparing each set-up's room-temperature value of the silicon Raman peak at 520 cm^{-1}. However, measuring a standard Si sample with the macro-Raman installation was infeasible since the MBE controller's setting that yielded room temperature at the manipulator was unknown.

In order to include the InSb data point at 527 °C into the calibration data, the positive offset between the 157 °C E_2 peak centers was subtracted from the peak center obtained at the melting point of InSb. Performing the offset correction on the E_2 phonon peak center at 527 °C, and adding the peak center's uncertainties of the In and InSb melting points, yielded a value of 777.45 ± 0.33 cm^{-1}. Peak fitting parameters of the hot-plate calibration spectra obtained with the 514.531 nm laser line are listed in Table 3.

Table 3: Laboratory Calibration Data

Temperature (^{0}C)	**Error (^{0}C)**	**Center (cm^{-1})**	**Error (cm^{-1})**	**Width (cm^{-1})**	**Error (cm^{-1})**
47.3	0.5	787.23	0.02	2.65	0.03
45.7	0.5	787.18	0.02	2.65	0.03
45.6	0.5	787.17	0.02	2.65	0.03
43.7	0.5	787.29	0.02	2.63	0.03
45.3	0.5	787.20	0.02	2.60	0.03
48.7	0.5	787.20	0.02	2.64	0.03
54.8	0.5	787.14	0.02	2.66	0.03
61.0	0.5	787.05	0.02	2.68	0.03
67.3	0.5	786.96	0.02	2.69	0.03
74.1	0.5	786.72	0.02	2.68	0.02
88.0	0.5	786.56	0.03	2.75	0.04
99.0	0.5	786.31	0.01	2.44	0.08
99.5	0.5	786.35	0.01	2.82	0.02
118.5	0.5	785.96	0.01	2.84	0.02
127.3	0.5	785.71	0.01	2.96	0.02
147.0	0.5	785.25	0.01	3.00	0.02
157.0	0.5	785.15	0.02	3.01	0.02
162.1	0.5	785.00	0.02	3.02	0.02

Support for the offset correction performed on the InSb data point is provided by comparing the E_2 phonon peak center obtained using Eq. 29 with a room temperature measurement acquired with the 514.531 nm laser line. Evaluating Eq. 29 at 25 °C with the parameters of ω_0 = 792.0 cm^{-1} and A = 3.0 cm^{-1} yields an E_2 phonon peak center of 787.72 cm^{-1}. Using a standard back-scattering Raman measurement configuration, the room-temperature value of the 6H-SiC E_2 phonon peak center was determined to be 787.51 ± 0.02 cm^{-1}. Evaluating Eq. 29 at 36 °C yields the room-temperature measurement's peak center. This is a reasonable difference when considering the 370 °C separation occurring between the 157 °C and 527 °C calibration points.

The temperature dependence of the E_2 line width is summarized in Fig. 14(b). As expected and seen in the raw data of Fig. 11, a gradual increase is observed in $\Gamma(T)$. This increase is due to the diminishing lifetime of the zone-center E_2 phonon resulting from impurity- and defect-related scattering and the anharmonic decay via phonon-phonon scattering.

From the calibration data and Eq. (41), fit parameter values of Γ_0 = 0.4 cm^{-1} and C = 1.4 cm^{-1} are obtained. Both values are in reasonable agreement with what has been previously reported.[12] It is noted that the gradual change in the line width of this phonon makes it less suitable than peak position for accurately estimating an unknown sample temperature.

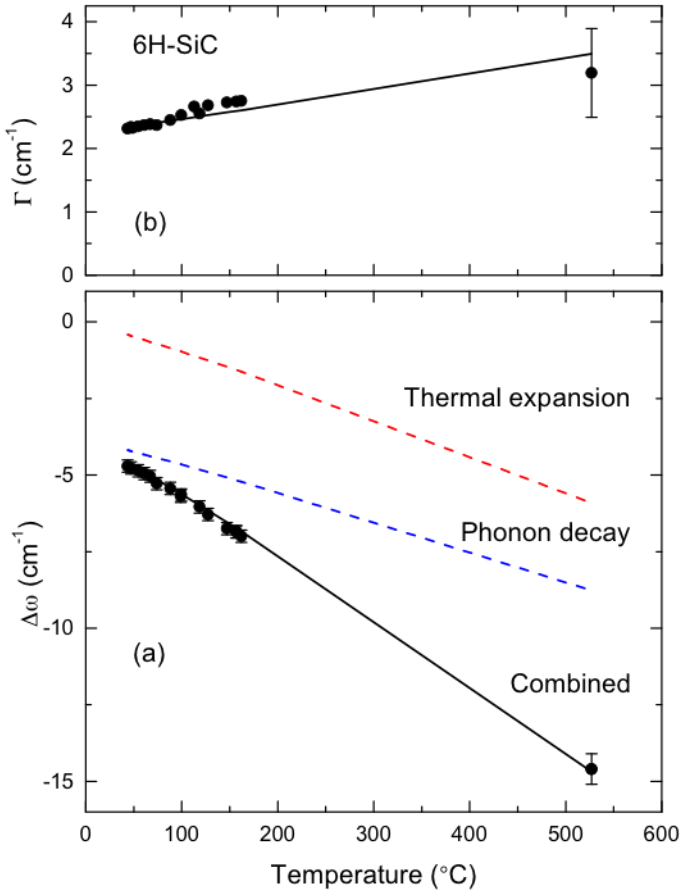

Figure 14: Laboratory and MBE Calibration Points. (a) Absolute change in the E_2 phonon peak position versus temperature. (b) E_2 phonon peak line width versus temperature. The black dots are the raw data points and each curve represents the predicted redshift discussed in section 4.5.

7.2 Repeatability of Raman-based Temperature Measurements

In order to determine the repeatability of the Raman-based method of temperature detection for the MBE growth chamber, two measurements of the same temperature controller setting were taken approximately one month apart and compared. CCD

calibrations at the MBE chamber were performed with the same set of Ne emission wavelengths, spectrometer slit width, and diffraction grating orientation within the spectrometer. A CCD calibration was performed before each round of measurements. The apparatus and spectrometer remained under the growth chamber between measurement periods, during which personnel performed routine MBE operations. Within the month of time separating each measurement, the 6H-SiC sample had been removed and re-installed into the MBE growth chamber multiple times using one of two, similarly shaped Mo sample holders.

The method's repeatability depended upon several variables arising from both inside and outside the MBE growth chamber. The external variable pertained to the amount of physical disturbance experienced by the spectrometer and macro-Raman optics throughout the month-long period separating the measurements. Subjecting the macro-Raman system to a sufficient physical disturbance could potentially misalign the spectrometer and optics. Any such misalignment would bring the scattered beam out of normal incidence with the spectrometer's slit and skew the incidence of the diffracted rays with the CCD detector. The resulting effect would be a net shift in peak features from their aligned positions. The internal variable was the thermal properties of the Mo sample holder utilized for the measurement and the amount of indium paste used secure the 6H-SiC sample. Even though the two Mo sample holders used during the experiment were similar in shape, operators of the MBE system relayed that differences in their thermal properties had been observed.

The repeatability of the experiment can be determined by exploiting a peak appearing in the Raman spectra that originates from the room's lights. Since the light's peak is temperature-independent, differences in its spectral position is directly attributable to disturbances of the macro-Raman apparatus or from the use of a different Mo sample holder. Comparing each measurement's value of the difference between the E_2 peak and the peak coming from the room's light yields a measure of the Raman-based temperature detection method's repeatability.

The two measurements used for comparison were obtained on 4/1/2014 and 5/6/2014 using different Mo sample holders. For both acquisitions, the manipulator's temperature controller was set to 300 °C and spectra were acquired once the readout of the controller temperature ceased to fluctuate. Each acquisition period was 120 s in duration and the spectrometer's slit width was set to 80 microns. On both dates the growth chamber pressure was approximately 8.0×10^{-11} Torr. The measurement performed on 04/01/2014 yielded a peak center of 790.78 ± 0.08 cm^{-1} for the E_2 phonon and a peak center of 484.63 ± 0.18 cm^{-1} for the room's light. For the measurement carried out on 05/06/2014, the E_2 phonon peak center was observed at 789.51 ± 0.08 cm^{-1} and the peak center of the ambient light was located at 484.09 ± 0.08 cm^{-1}. The E_2 phonon peaks were fit using a Lorentzian line shape and the background peaks were fit with a Voigt-area approximation line shape. Also, the r^2 values of the fits ranged from 0.98 to 0.99. Since the room light is expected to be unaffected by the Raman alignment, we may consider it to be an internal calibration. Since the offset from 4/1 to 5/6 is -0.54 ± 0.16

cm^{-1}, adjusting for this internal calibration results in a Raman shift of the 790 cm^{-1} line of +0.73 ± 0.32 cm^{-1}. This shift corresponds to a temperature of 34 ± 15 °C.

At a controller setting of 300 °C, the difference between the centers of the E_2 Raman peak and light's peak for the 4/1/2014 and 5/6/2014 measurements are 306.15 ± 0.26 cm^{-1} and 305.42 ± 0.35 cm^{-1}, respectively. The two measurements are offset by 0.73 ± 0.61 cm^{-1}. Once again taking into account the offset of the internal calibration line of the room lights, the difference in the 306 cm^{-1} line is 0.19 ± 0.77 cm^{-1}. The previously mentioned internal and external variables that affect the method's repeatability and encountered during the month-long period separating each measurement are clearly an undesirable effect. Under ideal conditions, the internal calibration approach should result in a temperature offset within uncertainty of zero. Future implementation of the method should rely on more than one internal calibration line to improve accuracy. Furthermore, minimizing disturbances in the apparatus's environment and utilizing a consistent sample holder configuration will increase repeatability of the Raman-based temperature detection method.

7.3 Standard Temperature Ramp

Fig. 15 compares temperature of the thermocouple, used for control, and the Raman results during the ramp process. Straightforward conclusions may be drawn from comparing these results. First, temperature is overestimated by the thermocouple reading by ~ 100 °C. Second, the ramp rate at the substrate (albeit delayed) is comparable to that at the thermocouple, suggesting that parasitic heat losses are a consistent factor for these

ramp conditions. Third, there is a time lag as large as 10 min between the thermocouple temperature reaching the set point (550 °C) and the substrate achieving near steady-state conditions at its much lower temperature. An additional 10 min soak resulted in a flat temperature profile at 400 °C, but did not address the temperature differences between these two sensing approaches.

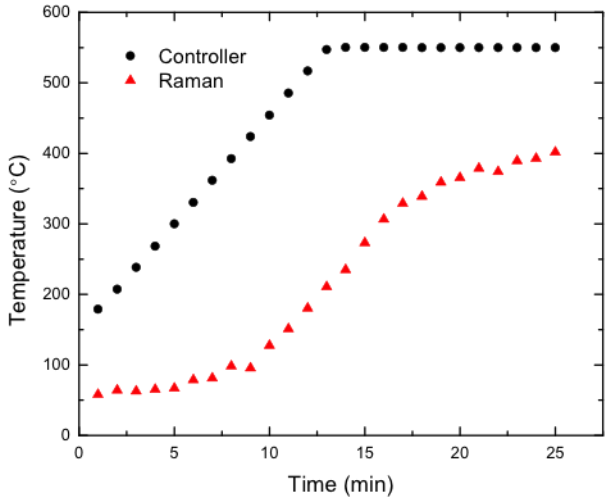

Figure 15: Comparison of Thermocouple and Raman Measurement Temperatures. Comparison between thermocouple measurements reported by the controller and the corresponding Raman temperatures acquired during the standard temperature ramp process.

8. CONCLUSION

In summary, an *in situ* temperature measurement based on Raman scattering has been successfully demonstrated and implemented in a standard MBE growth system. Measurements were performed with an apparatus built from standard optical components and a commercially available camera objective. Calibration was carried out using combined data measured with a representative 6H-SiC substrate in a laboratory setting and MBE system. The available capabilities permitted the qualification of the approach from room temperature to 527 °C. To examine the efficacy of this method for absolute measurement of temperature, the method was applied to a standard MBE ramp process. Results show that the thermocouple significantly overestimates the substrate temperature by ~ 100 °C and that there is a > 10 min delay in achieving steady state at the sample relative to the controller.

LITERATURE CITED

[1] M. Henini, Molecular Beam Epitaxy: From Research to Mass Production (Oxford: Elsevier, 2013).

[2] W. M. Haynes, Handbook of Chemistry and Physics (CRC Press 2011) 92nd ed. pp. 4.121 - 4.123.

[3] H. Morkoc, J. Appl. Phys. **76**, 1363 (1994).

[4] A. J. SpringThorpe, S. J. Ingrey, B. Emmerstorfer, P. Mandeville, App. Phys. Lett. **50**, 77-79 (1987).

[5] R. N. Sacks, D. Barlett, C. A. Taylor, and J. Williams, J. Vac. Sci. Technol. B **23**, 1247 (2005).

[6] P. Weightman, D. S. Martin, R. J. Cole, and T. Farrell, Reports on Progress in Physics **68**, 1251 (2005).

[7] S. K. Sharma, P. G. Lucey, M. Ghosh, H. W. Hubble, and K. A. Horton, Spectrochimica Acta Part a-Molecular and Biomolecular Spectroscopy **59**, 2391 (2003).

[7] L. C. Pacheco-Londono, W. Ortiz-Rivera, O. M. Primera-Pedrozo, S. P. Hernandez-Rivera, Analytical and Bioanalytical Chemistry **395**, 323 (2009).

[8] D. R. T. Zahn, A. Schneider, and D. Drews, J. Raman Spectroscopy **28**, 825 (1997).

[8] M. Kuball, Surface and Interface Analysis **31**, 987 (2001).

[9] C. Kittel, Introduction to Solid State Physics (Wiley & Sons, New York 1996) 7th Edition.

[10] B. Mihailova, "Raman and IR spectroscopy in materials. Symmetry analysis of normal phonon modes," University of Hamburg, Institute of Mineralogy and Petrology, Lekeito, Spain, 21-27 June 2009.

[11] M. S. Dresselhaus, "Applications of Group Theory to the Physics of Solids," Spring 2002.

[12] I. Ahmad, V. Kasisomayajula, D. Y. Song, L. Tian, J. M. Berg, M. Holtz, J. Appl. Phys. **100**, 113718 (2006).

[13] D. Y. Song, S. A. Nikishin, M. Holtz, V. Soukhoveev, A. Usikov, V. Dimitriev, J. Appl. Phys. **101**, 053535 (2007).

[14] W. Hayes, R. Loudon, Scattering of Light By Crystals (John Wiley & Sons, New York 1978).

[15] J. D. Jackson, Classical Electrodynamics (John Wiley & Sons, USA 1999).

[16] H. Ashraf, Masters of Science, Linkoping University, 2005.

[17] R. Cheung, Silicon Carbide Microelectromechanical Systems for Harsh Environments (Imperial College Press, 2006).

[18] M. Bauer, A. M. Gigler, A. J. Huber, R. Hillenbrand, R. W. Stark, J. Raman Spectrosc. **40**, 1867-1874 (2007).

[19] J. Liu, Y. K. Vorha, Phys. Rev. Lett. **77**, 1661 (1996).

[20] Z. Li, R.C. Brandt, J. American Ceramic Society **70**, 15.

[21] J. S. Steinhart, S. R. Hart, Deep Sea and Oceanographic Abstracts **15**, 497-503 (1968).

[22] G. W. Burns, M. G. Scroger, G. F. Strouse, M. C. Croukin, W. F. Guthrie, NIST Monograph 175 (1993).

[23] O. Madelung, U. Rössler, M. Schulz, Landolt-Börnstein - Group III Condensed Matter, (Springer Berlin Heidelberg 2002) Volume 41, Subvolume A1b, pp.1-6.